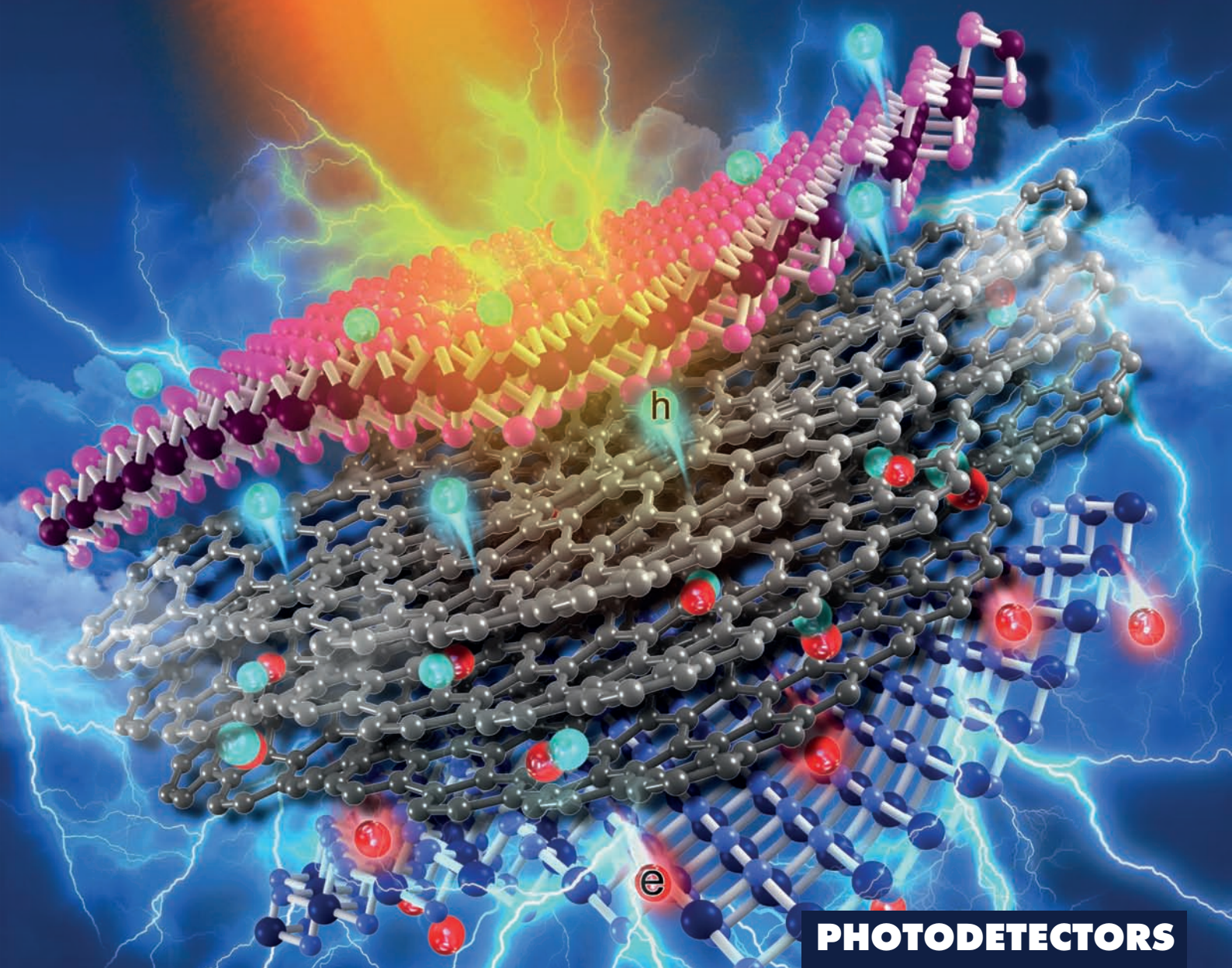


ADVANCED MATERIALS



PHOTODETECTORS

In article number 1805656, Rui Chen, Liyuan Zhang, Youpin Gong, and co-workers develop an h-BN/MoTe₂/graphene/SnS₂/h-BN van der Waals heterostructure to realize an ultrahigh-sensitivity broadband (405–1550 nm) photodetector, due to its unique advantages for high-efficiency light absorption and exciton dissociation. Graphene plays a key role in enhancing the sensitivity and broadening the spectral range, providing a viable approach toward future ultrahigh sensitivity and broadband photodetectors.

Ultrahigh-Sensitive Broadband Photodetectors Based on Dielectric Shielded MoTe₂/Graphene/SnS₂ p–g–n Junctions

Alei Li, Qianxue Chen, Peipei Wang, Yuan Gan, Tailei Qi, Peng Wang, Fangdong Tang, Judy Z. Wu, Rui Chen,* Liyuan Zhang,* and Youpin Gong*


2D atomic sheets of transition metal dichalcogenides (TMDs) have a tremendous potential for next-generation optoelectronics since they can be stacked layer-by-layer to form van der Waals (vdW) heterostructures. This allows not only bypassing difficulties in heteroepitaxy of lattice-mismatched semiconductors of desired functionalities but also providing a scheme to design new optoelectronics that can surpass the fundamental limitations on their conventional semiconductor counterparts. Herein, a novel 2D h-BN/p-MoTe₂/graphene/n-SnS₂/h-BN p–g–n junction, fabricated by a layer-by-layer dry transfer, demonstrates high-sensitivity, broadband photodetection at room temperature. The combination of the MoTe₂ and SnS₂ of complementary bandgaps, and the graphene interlayer provides a unique vdW heterostructure with a vertical built-in electric field for high-efficiency broadband light absorption, exciton dissociation, and carrier transfer. The graphene interlayer plays a critical role in enhancing sensitivity and broadening the spectral range. An optimized device containing 5–7-layer graphene has been achieved and shows an extraordinary responsivity exceeding 2600 A W⁻¹ with fast photoresponse and specific detectivity up to ≈10¹³ Jones in the ultraviolet–visible–near-infrared spectrum. This result suggests that the vdW p–g–n junctions containing multiple photoactive TMDs can provide a viable approach toward future ultrahigh-sensitivity and broadband photonic detectors.

Photodetectors capable of detecting light in a wide spectrum is central to diversified optoelectronic applications in spectroscopy, remote sensing, imaging and optical communication.^[1] Two-dimensional (2D) transition metal dichalcogenides (TMDs) provide a tremendous potential for broadband optoelectronics due to their relatively high mobility, appropriate bandgaps, and flexibility.^[2–18] In particular, TMD layers of different bandgaps and doping (p or n types) can be stacked together into van der

Waals (vdW) heterostructures to enable broadband optoelectronics,^[19–24] which has been a major hurdle in epitaxy of conventional semiconductors of different bandgaps.^[25,26] The vdW p–n heterostructure has several unique advantages: 1) it can contain multiple photoactive layers with different and complementary optical absorption spectra; 2) a p–n junction can be formed by stacking a p-type and an n-type 2D TMD layers for efficient dissociation of the excitons (photoexcited electron–hole pairs) by the vertical built-in electrical field across the p–n junction; and 3) the potential barrier at the p–n junction can efficiently inhibit the random carriers transport, leading to a low level of noise in the device. These advantages have motivated a large number of works to explore vdW p–n junctions, such as MoTe₂/MoS₂,^[14,27] WSe₂/MoS₂,^[28] WSe₂/SnS₂,^[29,30] black phosphorous (BP)/MoS₂,^[31,32] and WS₂/MoS₂^[33] for photodetection. Although these photodetectors exhibit a promising on/off current ratio (10³–10⁵) and detectivity (D^* , up to 10¹⁰–10¹¹ Jones in near infrared (NIR), where 1 Jones = 1 cm Hz^{1/2} W⁻¹), the responsivity (R_i) is fairly low (0.01–1.0 A W⁻¹ in NIR).^[2] For example, photovoltaic MoS₂/black phosphorus vertical vdW p–n diode can reach an on/off current ratio of ≈10³ and D^* value of ≈10⁹ Jones under 1550 nm laser illumination, respectively, while the R_i is only ≈153.4 mA W⁻¹ (1550 nm laser).^[32] In addition, most of the reported vdW p–n junction devices are narrowband operating primarily in the visible spectrum only.^[2] It is therefore important to realize both high detectivity

A. L. Li, Q. X. Chen, Dr. P. P. Wang, Y. Gan, T. L. Qi, P. Wang, F. D. Tang, Prof. L. Y. Zhang, Prof. Y. P. Gong
Department of Physics
Southern University of Science and Technology
Shenzhen 518055, China
E-mail: zhangly@sustc.edu.cn; gongyp@sustc.edu.cn

A. L. Li
Department of Physics
Harbin Institute of Technology
Harbin 150001, China

 The ORCID identification number(s) for the author(s) of this article can be found under <https://doi.org/10.1002/adma.201805656>.

DOI: 10.1002/adma.201805656

Prof. J. Z. Wu
Department of Physics and Astronomy
University of Kansas
Lawrence, KS 66045, USA

Prof. R. Chen, Prof. Y. P. Gong
Department of Electrical and Electronic Engineering
Southern University of Science and Technology
Shenzhen 518055, China
E-mail: chenr@sustc.edu.cn

Prof. Y. P. Gong
SUSTech Academy for Advanced Interdisciplinary Studies
Southern University of Science and Technology
Shenzhen 518055, China

by increasing the photoresponsivity and broadband through the design of vdW p–n junctions with photoactive 2D layers beyond the visible spectrum.

In this work, we present the first h-BN/MoTe₂/graphene/SnS₂/h-BN vdW p–g–n junction by introducing a graphene (g) interlayer using a layer-by-layer dry transfer method and demonstrate its ultrahigh-sensitive and broadband photodetection. MoTe₂ is a p-type semiconductor with the 2H structure (trigonal prismatic) and a bandgap of ≈1.0 eV while SnS₂ is an n-type semiconductor with a bandgap of ≈2.2 eV. Therefore, MoTe₂ and SnS₂ are particular suitable candidates for broadband vdW p–n heterojunction optoelectronics due to their high carrier mobility, complementary bandgaps and chemical stability.^[9,34–42] Furthermore, the introduction of a graphene-interlayer in the vdW p–g–n junction may improve the contact between the TMD layers to facilitate electron transport for higher R_i and to reduce the interface charge traps for faster photoresponse.^[16,43,44] In addition, light absorption, mobility, and transport distance of photoinduced carriers-to-electrodes can be efficiently tuned and optimized by varying the thickness of the graphene interlayer, which has an important effect on the optoelectronic performance of the vdW p–g–n junction devices such as R_i and photoresponse speed. Finally, the h-BN sandwich structure provides an additional screening effect to reduce or diminish the detrimental impact of the charged impurities from the substrate surface or the environment contamination

on the device response time and noise spectrum. This h-BN/MoTe₂/graphene/SnS₂/h-BN vdW heterojunction photodetector exhibits an unprecedented R_i and D^* over a wide spectrum ranging from ultraviolet (UV) to short-wave infrared (SWIR). In particular, the R_i and the D^* of the photodetector can reach up to $2.64 \times 10^3 \text{ A W}^{-1}$ and 1.1×10^{13} Jones under 1064 nm light illumination at room temperature, respectively, which surpasses not only the previously reported value in 2D vdW vertical heterostructures photodetectors by more than two orders of magnitude,^[2,5,45] but also are superior to the current state-of-the-art commercial infrared photodetectors ($\approx 10^{12}$ Jones) requiring cryogenic cooling.^[26] The D^* up to 1.06×10^{11} Jones under 1550 nm SWIR excitation at room temperature is also nearly 2 orders of magnitude larger than that of the previously reported on the 2D vdW vertical junctions^[2,32] and even comparable with commercial SWIR photodetectors such as uncooled Ge-on-Si photodetectors.^[46–48]

The operating principle of the h-BN/MoTe₂/graphene/SnS₂/h-BN vdW p–n junction photodetector can be understood through the 3D device configuration and band diagram of the heterostructure shown in **Figure 1**. The top and back h-BN flakes are used to isolate the MoTe₂/graphene/SnS₂ heterostructure from the environment (Figure 1a), which is designed to improve the performance of the photodetector. Figure 1b presents an optical image of an h-BN/MoTe₂/graphene/SnS₂/h-BN heterostructures devices. Few-layer SnS₂, MoTe₂,

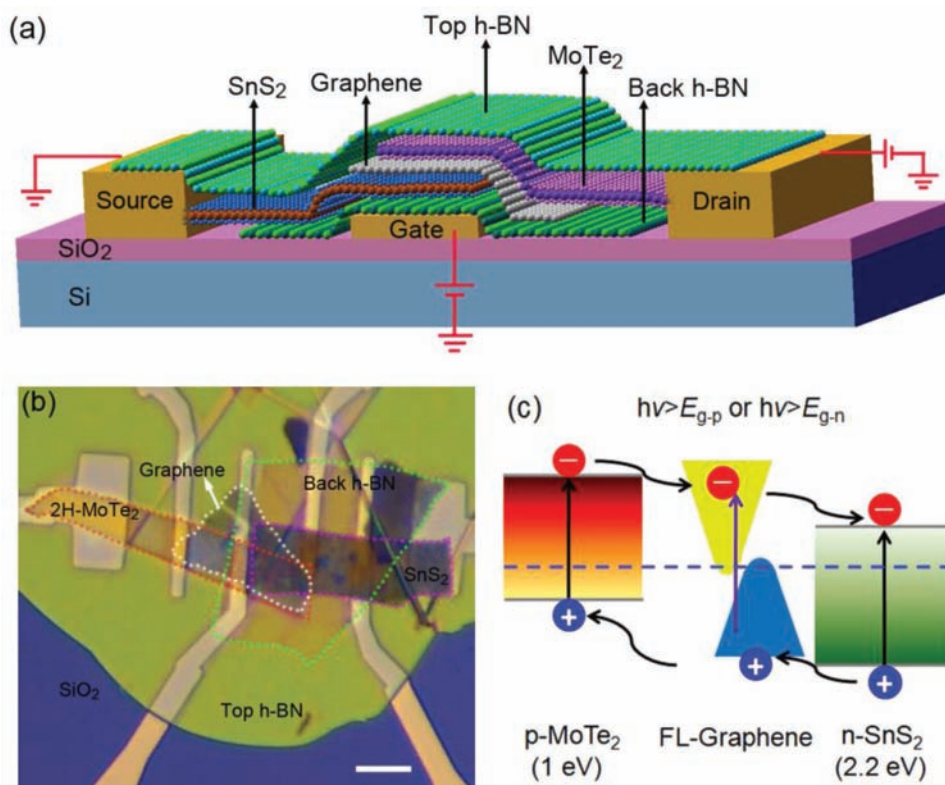


Figure 1. Stacked h-BN/MoTe₂/graphene/SnS₂/h-BN van der Waals heterostructures for broadband photodetection. a) Schematic h-BN/MoTe₂/graphene/SnS₂/h-BN device configuration and the experimental setup. b) Optical image of a typically fabricated device. Scale bar, 6 μm . c) Schematic band diagram and photoexcited carriers transport of the MoTe₂/graphene/SnS₂ vdW heterostructures. The E_{g-p} and E_{g-n} represent the band gap of p-MoTe₂ and n-SnS₂, respectively. Here, FL-graphene is a semi-metallic property which the Fermi level (at absolute zero) locates at above the bottom of the conduction band and below the top of the valence band due to the overlap of the conduction and valence bands.

graphene and h-BN flakes were obtained by the mechanical exfoliation and stacked sequentially as described in the Experimental Section. Atomic force microscopy (AFM) was applied to determine the thicknesses of the constituent layers of MoTe₂, graphene, and SnS₂ to be ≈4.3 (5 layers), ≈3.1 nm (7 layers), and ≈4.8 nm (5 layers), respectively (Figure S1a, Supporting Information). The crystalline quality of the TMDs and vdW heterojunction was confirmed by Raman spectroscopy under 532 nm laser excitation (Figure S1b,c, Supporting Information). Figure 1c depicts the band diagram of the MoTe₂/graphene/SnS₂ vdW heterostructure and the working principle of the device upon optical illumination. The $E_{g-p} = 1$ eV and $E_{g-n} = 2.2$ eV represent the band gap of p-MoTe₂ and n-SnS₂ (Figure S2a,b, respectively, in the Supporting Information), corresponding to the absorption band edges of 1240 nm and 563 nm, respectively. To equilibrate the Fermi level, the energy band of the MoTe₂/graphene/SnS₂ vdW p–n junction is tilted toward the n-SnS₂ layer (Figure 1c). When the incident photon energy is greater than the bandgaps of TMDs, all photoactive layers (MoTe₂/graphene/SnS₂) can absorb photons to generate the photogenerated carriers, and the electrons will move toward the SnS₂ while holes to MoTe₂. When the wavelength of the incident light is longer than 1240 nm, the graphene would be the only remaining light absorber. This photogating effect (light-induced electric field that causes charge doping into a semiconductor) is unique at the interface with

semiconductor quantum dots, 2D TMDs, carbon nanotubes or other nanostructures due to the strong quantum confinement and therefore significantly enhanced exciton lifetime in these low-dimensional nanomaterials.^[49–51] With assistance of the built-in electric field designed at the interface with these low-dimensional nanostructures, excitons dissociate into electrons and holes and one of them can be transfer out across the interface. Consequently, the trapped opposite charges generate a gating effect, the so-called photogating before the annihilation of the excitons. Obviously, in our devices, the heterojunctions composed of multiple photoactive layers play a key role in efficiently separating photoexcited electron–hole pairs into free charge carriers which contribute to a strong photoresponse and a wide spectral photodetection.

The electrical transport characteristics and photoresponse of the devices were measured and the result is shown in Figure 2a and Figure S3 in the Supporting Information. The current–voltage (I_{ds} – V_{ds}) curves across the MoTe₂/graphene/SnS₂ vertical junction by applying different gate voltage (V_g) on the h-BN back-gate dielectric show that the I_{ds} changes with changing gate voltage (Figure 2a) with a current on/off ratio near 2×10^2 (Inset in Figure 2a, Figure S3b in the Supporting Information), which demonstrates that the carrier concentration of MoTe₂/graphene/SnS₂ junction can be tuned by applying gate voltages (for more details, see the caption of Figure S3 in the Supporting Information). In addition, considering the low-power

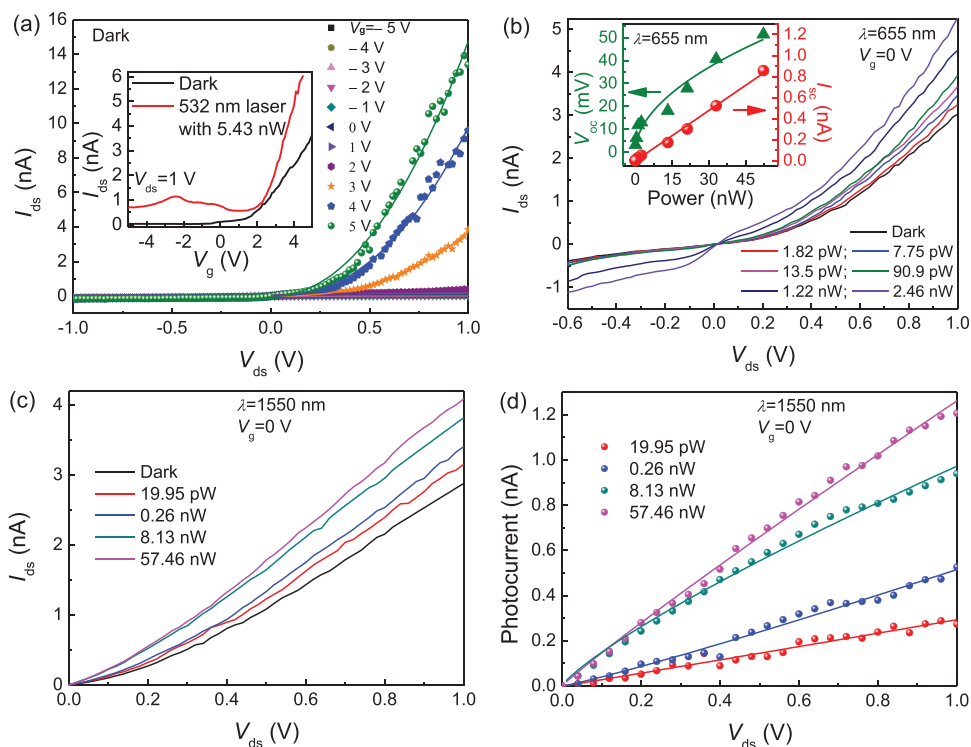


Figure 2. Transport properties and optoelectronic characterization of the h-BN/MoTe₂/graphene/SnS₂/h-BN van der Waals heterostructures. a) I_{ds} – V_{ds} curves of the device in the dark measured at various V_g from -5 to 5 V by applying voltage on the h-BN. Inset: I_{ds} – V_g curves of the device in dark and under 532 nm laser illumination measured at $V_{ds} = 1$ V. b) I_{ds} – V_{ds} curves of the devices in dark and under light illumination with different light powers at $V_g = 0$ V. The laser wavelength is 655 nm. The inset shows extracted open-circuit voltage (V_{oc} , left axis) and short-circuit current (I_{sc} , right axis) as functions of light illumination power ($V_g = 0$ V). c) I_{ds} – V_{ds} curves of the devices in the dark and under light illumination with different light powers with excitation wavelength at 1550 nm. d) I_p – V_{ds} curves for different light illumination powers with excitation wavelength at 1550 nm, showing a linear dependence on the bias ($V_g = 0$ V).

requirements of device operation and the gate tunability is typically not necessary in photodiodes, $V_g = 0$ is selected in the optoelectronic measurements in this work. Figure 2b shows typical $I_{ds}-V_{ds}$ curves of the heterostructures in dark and under different illumination powers with excitation wavelength of 655 nm. An anticipated rectifying behavior for a p–n junction was observed, confirming that the expected p–n junction is successfully formed in the vertical MoTe₂/graphene/SnS₂ vdW heterostructure.

The p–n junction characteristics are further confirmed by the photovoltaic effect under various excitation wavelengths ranging from 532 nm to 1064 nm (Figure S4, Supporting Information). The performance of the broadband photodetection of the devices can be evaluated from the photoresponse under light illumination with different wavelengths. Figure 2c plots the $I_{ds}-V_{ds}$ curves of the heterostructures in dark and under light illumination at the excitation wavelength of 1550 nm. In order to compare with the reported detector performance, we will mainly focus on the optoelectronic performance under the small V_{ds} range from 0 to 1 V. The I_{ds} is also nonlinear even at low biases in the range of 0–1 V and a strong photoresponse is demonstrated in a wide spectrum (also see Figure S5a,c,e, Supporting Information), which is attributed to p–n junction properties. Moreover, the photovoltaic effect is discovered when $I_{ds}-V_{ds}$ curves are zoomed into the minimal bias region of 0.1 V (Figure S4a, Supporting Information). The extracted open-circuit voltage (V_{oc} , left axis) and short-circuit current (I_{sc} , right axis) increase exponentially and linearly, respectively, with increasing the incident light power (Inset in Figure 2b,

Figure S4b–e in the Supporting Information), which is consistent with photovoltaic properties in p–n junctions solar cells. It is worth noting that the V_{oc} and I_{sc} are negligible at the excitation wavelength of 1550 nm (Figure S4f, Supporting Information). This can be explained by the above-mentioned mechanism that only graphene acts as a light absorbing medium when the photon energy is smaller than $E_{g-p} = 1.0$ eV, since the photoresponse of graphene is mainly through the photoconductive mechanism (i.e., linear $I_{ds}-V_{ds}$) that is distinguished from the photovoltaic mechanism.^[5] Additionally, the photocurrent ($I_p = I_{light} - I_{dark}$ is defined as the difference between the light-current I_{light} and dark-current I_{dark}) exhibits a linear dependence on the bias voltage V_{ds} (Figure 2d, and Figure S5d,f in the Supporting Information), implying higher photocurrent can be readily obtained by increasing the bias voltage. Notably, there is one exception in the case of devices under 405 nm light illumination, in which the photocurrent depends exponentially on the bias V_{ds} (Figure S5b, Supporting Information). This may be because that photon energy at UV region is so high that a large amount of photoexcited electron–hole pairs are generated in a short time and rapidly converted to photocurrent under a small bias voltage. This effect is also reflected in the subsequent discussion about dynamic photoresponse.

To gain further insights in the performance of the h-BN/MoTe₂/graphene/SnS₂/h-BN vdW heterostructure photodetectors, the light illumination power dependence of the photocurrent at various wavelengths from UV to SWIR is illustrated in Figure 3a and Figure S6 (Supporting Information). The responsivity R_i is an important parameter to evaluate

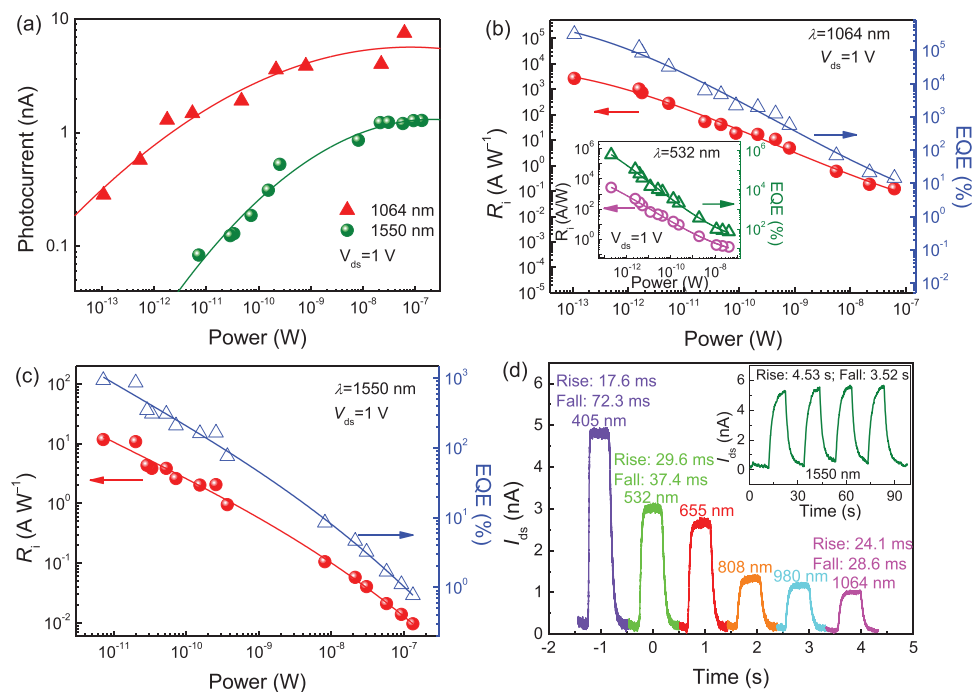


Figure 3. Photoresponse of the h-BN/MoTe₂/graphene/SnS₂/h-BN van der Waals heterostructures. a) Power dependence of photocurrent at wavelengths of 1064 and 1550 nm. b) Responsivity (left axis) and external quantum efficiency EQE (right axis) versus light illumination power with excitation wavelength at 1064 nm, showing the high sensitivity of the devices, with direct measurement of 0.1 pW. Inset: responsivity as functions of light power of the device at the excitation wavelength of 532 nm. $V_g = 0$ V and $V_{ds} = 1$ V. c) R_i (left axis) and EQE (right axis) versus light illumination power at excitation wavelength of 1550 nm at $V_g = 0$ V and $V_{ds} = 1$ V. d) Temporal photocurrent response under various wavelengths at 0.5 V bias from UV region (405 nm) to NIR (1064 nm) with the same order of magnitude optical power (42–62 nW). Inset: temporal photocurrent response under 1550 nm wavelength.

the performance of a photodetector and the R_i results of the photodetectors are shown in Figure 3b,c. The R_i can be calculated by $R_i = I_p/P_{in}$, where P_{in} is the incident light power received by the actual device with unit of W. Under the light illumination at both 1064 and 1550 nm laser wavelengths, the photocurrent at $V_{ds} = 1$ V increases monotonically with increasing illumination power at lower light powers up to 21 nW and reaches saturation at higher power (Figure 3a). Figure S7 (Supporting Information) shows that the R_i is tunable, that is, the higher R_i can be conveniently obtained by increasing bias voltage and decreasing light illumination power. Remarkably, the R_i of the devices reaches the values in exceeding 2.6×10^3 AW⁻¹ at $V_{ds} = 1$ V under low light illumination power for both 532 and 1064 nm excitation wavelengths, which is at least two orders of magnitude larger than that of the previous reports and represents the best so far achieved on the 2D/2D vdW p–n junctions NIR photodetectors (Table S1, Supporting Information). It is worth mentioning that the operating spectrum of the photodetectors reported in this work can extend to the telecommunication wavelength of 1550 nm with R_i up to 11.7 AW⁻¹ at 1 V bias (Figure 3c), which is comparable to the state-of-the-art commercial SWIR photodetectors.^[25,46,47] In addition, the photodetectors demonstrates a high sensitivity with a direct measurement of 0.1 pW under 532 nm (inset in Figure 3b) and 1064 nm light illumination (Figure 3b), which indicates that the built-in electric field in the MoTe₂/graphene/SnS₂ vdW heterostructure can efficiently separate excitons into photocurrent. The contribution of the built-in amplification mechanism in the p–g–n junctions is further clarified by calculating the EQE. The EQE is defined as the ratio of the number of photoexcited electron–hole pairs to the number of incident photons: $EQE = (I_p/e)/(P_{in}/h\nu)$, where h is Planck's constant, e is the electronic charge, and ν is the frequency of incident light. Similar to the dependence of the R_i on the bias voltage, the EQE increases as the incident light power decreases, and reaches the values ranging from 10% to 105% in a wide spectrum (from UV light to 1064 nm NIR) and close to 103% in the 1550 nm wavelength respectively (the right axis in Figure 3b,c). The EQE higher than 100% implies a large gain in the devices, which may be due to the driving of carriers by external voltage in the vertical device structure. Photoconductive gain could occur as a consequence of the photogating effect (one type of charge trapped at the interface due to 1–2 order of magnitude enhanced exciton life time), in combination of the short charge transit time of the opposite charge carriers in high mobility 2D materials. Considering this process is similar to that in photoconductors because the applied forward bias voltage V_{ds} (1 V) is much larger than the open-circuit voltage V_{oc} during the operation of the devices, the equation $G = \tau_c/\tau_t$ was employed to estimate the gain, where τ_c is the lifetime of photogenerated carriers that reside in the photoactive layers, and τ_t is the drift transit time of carriers across source–drain separation distance L . τ_t quantified by $\tau_t = L^2/(V_{ds}\mu)$, is governed by the external bias voltage. For our MoTe₂/graphene/SnS₂ vdW p–g–n heterostructure devices, the τ_t is on the order of 1 ns based on $\mu = 1\text{--}2$ cm² V⁻¹ s⁻¹ from the data in the inset of Figure 2a, $L = 12\text{--}30$ nm depended on different devices and $V_{ds} = 1$ V. Thus, this leads to the large gain G values between $\approx 10^4$ and $\approx 10^3$ by using $\tau_c = 54$ ms (405 nm) and $\tau_c = 20$ ms (1064 nm), respectively, from the

data obtained by a best fitted using a biexponential function in Figure 3d,^[52,53] which is in good agreement with the measured gain values. In our vertical p–g–n junction devices, the combination of the strong exciton binding energy, the short carrier transit distance, interlayer inelastic tunneling effect^[54,55] and the vertical built-in electric field across the p–g–n junction leads to the efficient excitons separation and rapid carrier transport (increased τ_c and reduced τ_t), which contribute the gain. (more details are discussion in the caption of Figure S7 in the Supporting Information).

The photocurrent switching is an important feature of the photodetectors that determines the photoresponse speed. On the h-BN/MoTe₂/graphene/SnS₂/h-BN vdW heterostructure photodetectors, the temporal photoresponse of the devices under modulated input light was measured at room temperature (Figure 3d, and Figure S8 in the Supporting Information). The rise (on) and fall (off) times can be obtained between 10% and 90% of the maximum photocurrent at the light on and off, respectively. Interestingly, the symmetry of rising time and falling time is different under light illumination with different excitation wavelengths. For 405 nm light illumination, the rise time and fall time are 17.6 and 72.3 ms, respectively, while they are 24.1 and 28.6 ms in response to NIR light (1064 nm) on and off respectively. Obviously, the dynamic photoresponse to light on and off are much more symmetric under the 1064 nm NIR illumination as compared to under UV light, which is consistent with previous analysis on the dependence of photocurrents on the bias. It is worth mentioning that the response speed of the h-BN/MoTe₂/graphene/SnS₂/h-BN vdW heterostructure photodetectors is comparable to and even faster than the recent reports on MoTe₂-based NIR photodetectors with the same order of magnitude R_i (Table S1, Supporting Information).^[38] The fast and symmetric switching response for NIR light in our photodetectors may be attributed to: 1) the p–n junction generates a vertical built-in electric field that reduces the charge trapping effect, 2) zero-bandgap graphene improves the interface contact of the semiconductor MoTe₂ and SnS₂ and reduces interface charge traps, which can rapidly transfers carriers separated by the built-in electric field, and 3) the screening effect of the h-BN sandwich structure on intrinsic or extrinsic charge traps. Note that an exception occurs, that is, the response speed under the 1550 nm illumination is suddenly slowed down to a few seconds (inset in Figure 3d). This is not surprising because the 1550 nm excitation wavelength exceeds the cutoff wavelength of both of MoTe₂ and SnS₂, in which case only graphene can absorb photons to produce carriers. Therefore, the response under 1550 nm illumination is essentially a graphene photodetector. Compared to the previously reported single graphene photodetectors,^[5] the responsivity of our devices has increased by several orders of magnitude despite the slower response, which can be attributed to the following two aspects: on the one hand, the built-in electric field derived from the p–n junction composed of MoTe₂ and SnS₂ significantly increases the exciton separation efficiency to generate a large photocurrent, which enhances the responsivity; but on the other hand, the distance from the carrier to the two electrodes is significantly increased because the 2D materials are inserted between the electrode and graphene, which slows the response speed.

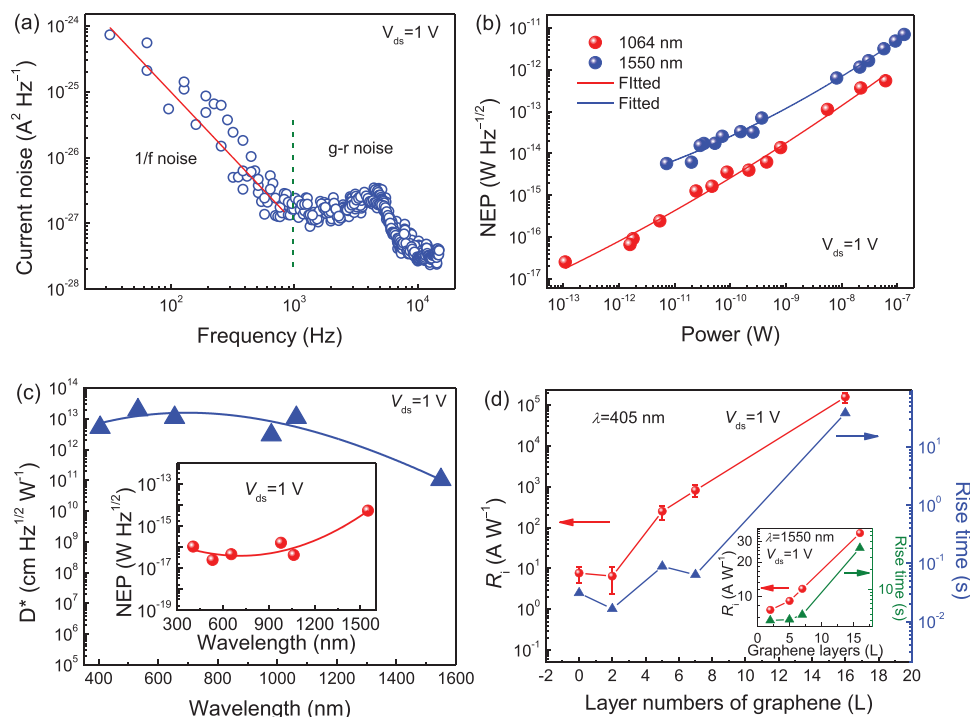


Figure 4. Broadband photodetection of the h-BN/MoTe₂/graphene/SnS₂/h-BN van der Waals heterostructures at the wavelengths ranging from ultra-violet region to NIR (communication band). a) Spectra of current noise power density (I_n^2) at $V_{ds} = 1$ V. The solid red line ($f > 1$ kHz) is a linear fit for the $1/f$ noise trend. b) NEP versus light illumination power with excitation wavelengths at 1064 nm (red) and 1550 nm (blue) at $V_{ds} = 1$ V. c) D^* and NEP (inset) at broadband ranging from 405 to 1550 nm at $V_g = 0$ V and $V_{ds} = 1$ V. d) R_i and response time under 405 nm illumination of the MoTe₂/SnS₂ and the MoTe₂/graphene/SnS₂ devices with various layer numbers of graphene interlayer. Inset: graphene thickness dependence of the R_i and response time under 1550 nm illumination. Measurements were carried out at $V_g = 0$ V.

To characterize the ultimate sensitivity of the photodetectors, we measured the spectra of current noise power density (I_n^2) under the dark at room temperature, as shown as in **Figure 4a**. Obviously, the I_n^2 as a function of the frequency (f) contains two typical regions. For the region of $f > 1$ kHz, the current noise can be fitted by $I_n^2 \propto 1/f$, which indicates that $1/f$ noise dominates the noise behavior of the photodetectors. The $1/f$ noise results from the random fluctuations of local electronic states affected by the surface quality of the materials such as defects or nonuniformity which exists in almost all detectors.^[26] While in the area of $f < 1$ kHz, the generation–recombination (g–r) noise originated from the random fluctuation of average carrier concentration dominates the noise behavior of the photodetectors, in which the current noise starts to maintain a level at low frequencies and then suddenly drops to a frequency. The noise equivalent power (NEP) is the optical input power required for the signal-to-noise ratio to be unity at the detector output. The NEP can be calculated by $NEP = \overline{i_n^2}^{1/2} / R_i = \text{RMS}(i_n) / R_i$ with unit of $\text{W Hz}^{-1/2}$, where $\text{RMS}(i_n)$ is the root mean square noise current with a value of 6.68×10^{-14} A $\text{Hz}^{-1/2}$ calculated from the spectra of noise power density. The current noise of the heterostructure photodetectors is quite low, which may be attributed to that the potential barrier at the p–n junction inhibits efficiently the random carriers transport,^[56] as well as the dielectric shielding effect of h-BN on the substrate and surrounding environment. Correspondingly, the calculated NEP values locate in the range of $\approx 10^{-17}$ – 10^{-16} $\text{W Hz}^{-1/2}$ at 1 V bias voltage under low light illumination power with the excitation

wavelengths of 405–1064 nm (Figure 4b, and Figure S9a–c in the Supporting Information), while the NEP has one order of magnitude increase (10^{-15} $\text{W Hz}^{-1/2}$) for the communication band of 1550 nm (Figure 4b, and Figure S9d in the Supporting Information). It should be pointed out that the NEP in our h-BN/MoTe₂/graphene/SnS₂/h-BN vdW p–g–n junction is at least 2–3 orders of magnitude lower than that of the previously reported in vdW p–n junctions.^[2,5,56]

Another important figure of merit related to the performance of a photodetector is the specific detectivity D^* that is independent of device area A (here A is $23.3 \mu\text{m}^2$), which is expressed as $D^* = A^{1/2} / NEP = R_i A^{1/2} / \overline{i_n^2}^{1/2}$. Particularly, an enhanced D^* is anticipated from the enhanced R_i or reduced NEP in our h-BN/MoTe₂/graphene/SnS₂/h-BN vdW p–g–n junction. Therefore, we calculated the D^* values at various excitation wavelengths ranging from 405 to 1550 nm at $V_{ds} = 1$ V (Figure 4c). The low NEP leads to a predicted high detection sensitivity. Similar to the relationship between NEP and excitation wavelength (inset in Figure 4c), the D^* shows a relatively homogeneous value of up to $\approx 10^{13}$ Jones under the excitation wavelengths from 405 to 1064 nm, while it declines to $\approx 10^{11}$ Jones at the excitation wavelength of 1550 nm. Remarkably, the D^* value is as high as up to 1.1×10^{13} Jones at excitation wavelengths of 1064 nm at room temperature, which represents not only nearly 2 orders of magnitude larger than that of the previously reported on 2D vdW vertical heterostructures photodetectors (Table S1, Supporting Information)^[2,5,45] but also is superior to state-of-the-art commercial NIR detectors such as

InGaAs photodetector with D^* of $\approx 10^{12}$ Jones while requiring cryogenic cooling at 4.2 K.^[26] The D^* value of 1.06×10^{11} Jones under 1550 nm excitation wavelengths is also nearly 2 orders of magnitude larger than that of the previously reported on the 2D vdW vertical junctions^[2,32] and even comparable with commercial SWIR photodetectors such as uncooled Ge-on-Si photodetectors.^[46–48] Further compared with the single MoTe₂-based NIR detector and single SnS₂-based visible light detector, the D^* of our devices surpasses the previously reported value in both photodetectors by at least two orders of magnitude (Table S1, Supporting Information).^[9,38,57,58] For conventional 3D semiconductors used as NIR and SWIR photodetection, they need to work at low temperatures because the noise at room temperature reduces their detectivity to an unacceptable level.^[25] Therefore, in recent years, Ge thin films were epitaxially grown on Si instead of single-crystal bulk Ge for making uncooled detectors for application in optical communications.^[46,47] In this work, the structure of the photodetector is a vertical 2D vdW heterojunction that combines two features: 1) it is a p–n junction and 2) it exists the dielectric shielding effect of back and top h-BN on the substrate and surrounding environment. As previously discussed, these two points play a key role in suppressing room-temperature noise. Therefore, our device can obtain a high D^* values in a wide spectrum even at room temperature. It is foreseeable that the performance of our device may be further improved if the temperature is cooled down during working. The extraordinary D^* in a wide spectrum ultimately demonstrates that our h-BN/MoTe₂/graphene/SnS₂/h-BN vdW heterostructure is a broadband photodetector with ultrahigh sensitivity.

To shed some lights on the roles of the sandwiching graphene and the origin of the high performances, the devices of the MoTe₂/SnS₂ and the MoTe₂/graphene/SnS₂ with various layer numbers of graphene interlayer were also fabricated by using the same stacking method. The R_i and response time of these devices under 405 nm illumination are shown in Figure 4d (main panel) and Figure S10 in the Supporting Information. To avoid other factors as much as possible, we mainly investigated the characteristics at an excitation wavelength of 405 nm which lies within the cutoff wavelength of all materials (MoTe₂/SnS₂ without graphene has no light response at 1550 nm; the cutoff wavelength of SnS₂ is 563 nm). The R_i of MoTe₂/graphene/SnS₂ with two-layer graphene interlayer is comparable to that of the MoTe₂/SnS₂, while the rise time of the former is slightly slower than the latter. This implies that the thin graphene interlayer improves the interface quality between the TMD layers and reduces the interface charge traps for faster photoresponse although thin layer (3 layers) graphene does not significantly increase R_i due to limited enhanced light absorption. Notably, both the R_i and rise time increase dramatically with further increasing layer numbers of graphene interlayer. For example, the R_i and rise time are $\approx 9 \text{ A W}^{-1}$ and $\approx 20 \text{ ms}$ with 2-layer graphene, $\approx 10^2\text{--}10^3 \text{ A W}^{-1}$ and $\approx 60\text{--}90 \text{ ms}$ with 5–7-layer graphene, and $\approx 10^5 \text{ A W}^{-1}$ and tens of seconds with 16-layer graphene interlayers, respectively. This indicates that the thickness of graphene interlayer has an important effect on the optoelectronic performance of the MoTe₂/graphene/SnS₂ devices including the light absorption and the interface engineering. The light absorption of single-layer graphene is only $\approx 2.3\%$, which means

the light absorption can be multiplied by increasing the layer numbers of graphene and is hence advantageous for enhancing the photoresponse of the device. Nevertheless, an increase in the layer number of graphene interlayer extends the transport distance of photoinduced carriers-to-electrodes and reduces the mobility, which could slow down the photoresponse. Thus, the higher R_i for the devices with 16-layer graphene interlayer are at the cost of slower photoresponse. On the contrary, the MoTe₂/graphene/SnS₂ devices with too thin graphene interlayer (3 layers) would result in a very small R_i due to an ultrashort carrier lifetime and low light absorption (2.3–4.6%), while the response speed is very fast. The graphene thickness dependence of the responsivity and response time under 1550 nm illumination (inset of Figure 4d) actually shows a similar feature with that under 405 nm illumination, although the responsivity and response speed of the former is significantly lower than the latter. Therefore, the optimized device structure of h-BN/MoTe₂/graphene/SnS₂/h-BN is the device containing 5–7-layer graphene, which has a large photoresponse ($\approx 10^2\text{--}10^3 \text{ A W}^{-1}$) and a relatively fast photoresponse speed (tens of milliseconds).

In summary, we have developed a novel h-BN/MoTe₂/graphene/SnS₂/h-BN vdW p–g–n junction using a layer-by-layer dry transfer method for uncooled broadband UV–vis–NIR photodetection. This device has several unique designs including 1) pairing p-type MoTe₂ (bandgap of $\approx 1.0 \text{ eV}$) with n-type SnS₂ (bandgap of $\approx 2.2 \text{ eV}$) for broadband light absorption; 2) insertion of a graphene interlayer between the MoTe₂ and SnS₂ to reduce the charge traps and to improve the interface quality, light absorption, as well as charge transport in the vdW p–g–n junction; and 3) implementation of an h-BN sandwich structure to screen the detrimental impact of the charged impurities from the substrate surface or the environment contamination on the device response time and noise spectrum. Moreover, the graphene interlayer plays a critical role in realizing both high photodetectivity and the photoresponsivity in a wide spectral range, and an optimized structure of the vdW p–g–n device containing 5–7-layer graphene interlayer have been achieved. The combined effect of these device designs is profound as illustrated in the extraordinary broadband R_i exceeding $2.6 \times 10^3 \text{ A W}^{-1}$ and D^* up to $\approx 10^{13}$ Jones. In particular, the D^* is up to 1.1×10^{13} Jones under 1064 nm NIR illumination at room temperature, which represents not only nearly two orders of magnitude larger than that of the previously reported on the MoTe₂-based NIR detectors, but also an enhancement of one order of magnitude over that of the state-of-the-art commercial InGaAs NIR detectors operated at extremely low temperatures near 4.2 K. Moreover, the D^* value of 1.06×10^{11} Jones at 1550 nm excitation is comparable with commercial SWIR photodetectors. Our study therefore illustrates that the vdW p–g–n junctions contained multiple photoactive 2D materials provide a viable route toward future ultrahigh-sensitivity and broadband optoelectronics.

Experimental Section

The detailed experimental process is stated in the Supporting Information, including the growth of MoTe₂ and SnS₂ bulk single crystals, the fabrication of the h-BN/MoTe₂/graphene/SnS₂/h-BN

vdW heterostructure photodetectors, and the characterization of optoelectronic performance.

Supporting Information

Supporting Information is available from the Wiley Online Library or from the author.

Acknowledgements

The work was supported by the Science and Technology Innovation Commission of Shenzhen Municipality (Grant Nos. JCYJ20170817110751776 and JCYJ20170307105434022) and the Guangdong Innovative and Entrepreneurial Research Team Program (Grant No. 2016ZT06D348). R.C. acknowledges the supports from national 1000 plan for young talents, the National Natural Science Foundation of China (Grant No. 11574130), and the Science and Technology Innovation Commission of Shenzhen Municipality (Grant Nos. KQJSCX20170726145748464 and JCYJ20150930160634263). J.Z.W. acknowledges US NSF contracts (Nos. NSF-DMR-1337737 and NSF-DMR-1508494) and the United States Army Research Office contract (No. ARO-W911NF-16-1-0029).

Conflict of Interest

The authors declare no conflict of interest.

Keywords

2D materials, broadband, photodetectors, transition-metal dichalcogenides, van der Waals heterostructures

Received: August 31, 2018

Revised: November 26, 2018

Published online: December 14, 2018

- [1] Q. L. Bao, K. P. Loh, *ACS Nano* **2012**, *6*, 3677.
- [2] C. Xie, C. Mak, X. M. Tao, F. Yan, *Adv. Funct. Mater.* **2017**, *27*, 1603886.
- [3] F. N. Xia, H. Wang, D. Xiao, M. Dubey, A. Ramasubramaniam, *Nat. Photonics* **2014**, *8*, 899.
- [4] T. J. Octon, V. K. Nagareddy, S. Russo, M. F. Craciun, C. D. Wright, *Adv. Opt. Mater.* **2016**, *4*, 1750.
- [5] F. H. L. Koppens, T. Mueller, P. Avouris, A. C. Ferrari, M. S. Vitiello, M. Polini, *Nat. Nanotechnol.* **2014**, *9*, 780.
- [6] F. Wang, Z. X. Wang, K. Xu, F. M. Wang, Q. S. Wang, Y. Huang, L. Yin, J. He, *Nano Lett.* **2015**, *15*, 7558.
- [7] S. C. Dhanabalan, J. S. Ponraj, H. Zhang, Q. L. Bao, *Nanoscale* **2016**, *8*, 6410.
- [8] E. F. Liu, M. S. Long, J. W. Zeng, W. Luo, Y. J. Wang, Y. M. Pan, W. Zhou, B. G. Wang, W. D. Hu, Z. H. Ni, Y. M. You, X. A. Zhang, S. Q. Qin, Y. Shi, K. Watanabe, T. Taniguchi, H. T. Yuan, H. Y. Hwang, Y. Cui, F. Miao, D. Y. Xing, *Adv. Funct. Mater.* **2016**, *26*, 1938.
- [9] X. Zhou, Q. Zhang, L. Gan, H. Q. Li, T. Y. Zhai, *Adv. Funct. Mater.* **2016**, *26*, 4405.
- [10] C. M. Huang, S. F. Wu, A. M. Sanchez, J. J. P. Peters, R. Beanland, J. S. Ross, P. Rivera, W. Yao, D. H. Cobden, X. D. Xu, *Nat. Mater.* **2014**, *13*, 1096.
- [11] Z. W. Zhang, P. Chen, X. D. Duan, K. T. Zang, J. Luo, X. F. Duan, *Science* **2017**, *357*, 788.
- [12] X. D. Duan, C. Wang, J. C. Shaw, R. Cheng, Y. Chen, H. L. Li, X. P. Wu, Y. Tang, Q. L. Zhang, A. L. Pan, J. H. Jiang, R. Q. Yu, Y. Huang, X. F. Duan, *Nat. Nanotechnol.* **2014**, *9*, 1024.
- [13] Y. Gao, Y. L. Hong, L. C. Yin, Z. T. Wu, Z. Q. Yang, M. L. Chen, Z. B. Liu, T. Ma, D. M. Sun, Z. H. Ni, X. L. Ma, H. M. Cheng, W. C. Ren, *Adv. Mater.* **2017**, *29*, 1700990.
- [14] A. Pezeshki, S. Hossein, H. Shokouh, T. Nazari, K. Oh, S. Im, *Adv. Mater.* **2016**, *28*, 3216.
- [15] H. Jeong, H. M. Oh, A. Gokarna, H. Kim, S. J. Yun, G. H. Han, M. S. Jeong, Y. H. Lee, G. Lerondel, *Adv. Mater.* **2017**, *29*, 1700308.
- [16] H. J. Tan, W. S. Xu, Y. W. Sheng, C. S. Lau, Y. Fan, Q. Chen, M. Tweedie, X. C. Wang, Y. Q. Zhou, J. H. Warner, *Adv. Mater.* **2017**, *29*, 1702917.
- [17] H. Xu, X. Han, X. Dai, W. Liu, J. Wu, J. Zhu, D. Kim, G. Zou, K. A. Sablon, A. Sergeev, Z. Guo, H. Liu, *Adv. Mater.* **2018**, *30*, 1706561.
- [18] M. S. Long, E. F. Liu, P. Wang, A. Y. Gao, H. Xia, W. Luo, B. G. Wang, J. W. Zeng, Y. J. Fu, K. Xu, W. Zhou, Y. Y. Lv, S. H. Yao, M. H. Lu, Y. F. Chen, Z. H. Ni, Y. M. You, X. A. Zhang, S. Q. Qin, Y. Shi, W. D. Hu, D. Y. Xing, F. Miao, *Nano Lett.* **2016**, *16*, 2254.
- [19] K. Kang, K. H. Lee, Y. M. Han, H. Gao, S. E. Xie, D. A. Muller, J. Park, *Nature* **2017**, *550*, 229.
- [20] P. Rivera, K. L. Seyler, H. Y. Yu, J. R. Schaibley, J. Q. Yan, D. G. Mandrus, W. Yao, X. D. Xu, *Science* **2016**, *351*, 688.
- [21] K. S. Thygesen, *2D Mater.* **2017**, *4*, 022004.
- [22] N. R. Wilson, P. V. Nguyen, K. Seyler, P. Rivera, A. J. Marsden, Z. P. L. Laker, G. C. Constantinescu, V. Kandyba, A. Barinov, N. D. M. Hine, X. D. Xu, D. H. Cobden, *Sci. Adv.* **2017**, *3*, e1601832.
- [23] F. Barati, M. Grossnickle, S. S. Su, R. K. Lake, V. Aji, N. M. Gabor, *Nat. Nanotechnol.* **2017**, *12*, 1134.
- [24] M. Massicotte, P. Schmidt, F. Violla, K. G. Schadler, A. Reserbat-Plantey, K. Watanabe, T. Taniguchi, K. J. Tielrooij, F. H. L. Koppens, *Nat. Nanotechnol.* **2016**, *11*, 42.
- [25] A. Rogalski, *Prog. Quantum Electron.* **2003**, *27*, 59.
- [26] J.-M. Liu, *Photonic Devices*, Cambridge University Press, New York, USA **2005**.
- [27] K. A. Zhang, T. N. Zhang, G. H. Cheng, T. X. Li, S. X. Wang, W. Wei, X. H. Zhou, W. W. Yu, Y. Sun, P. Wang, D. Zhang, C. G. Zeng, X. J. Wang, W. D. Hu, H. J. Fan, G. Z. Shen, X. Chen, X. F. Duan, K. Chang, N. Dai, *ACS Nano* **2016**, *10*, 3852.
- [28] R. Cheng, D. H. Li, H. L. Zhou, C. Wang, A. X. Yin, S. Jiang, Y. Liu, Y. Chen, Y. Huang, X. F. Duan, *Nano Lett.* **2014**, *14*, 5590.
- [29] Y. Wang, W. X. Zhou, L. Huang, C. X. Xia, L. M. Tang, H. X. Deng, Y. T. Li, K. Q. Chen, J. B. Li, Z. M. Wei, *2D Mater.* **2017**, *4*, 025097.
- [30] T. F. Yang, B. Y. Zheng, Z. Wang, T. Xu, C. Pan, J. Zou, X. H. Zhang, Z. Y. Qi, H. J. Liu, Y. X. Feng, W. D. Hu, F. Miao, L. T. Sun, X. F. Duan, A. L. Pan, *Nat. Commun.* **2017**, *8*, 1906.
- [31] Y. X. Deng, Z. Luo, N. J. Conrad, H. Liu, Y. J. Gong, S. Najmaei, P. M. Ajayan, J. Lou, X. F. Xu, P. D. Ye, *ACS Nano* **2014**, *8*, 8292.
- [32] L. Ye, H. Li, Z. F. Chen, J. B. Xu, *ACS Photonics* **2016**, *3*, 692.
- [33] Y. Z. Xue, Y. P. Zhang, Y. Liu, H. T. Liu, J. C. Song, J. Sophia, J. Y. Liu, Z. Q. Xu, Q. Y. Xu, Z. Y. Wang, J. L. Zheng, Y. Q. Liu, S. J. Li, Q. L. Bao, *ACS Nano* **2016**, *10*, 573.
- [34] H. P. C. Miranda, S. Reichardt, G. Froehlicher, A. Molina-Sanchez, S. Berciaud, L. Wirtz, *Nano Lett.* **2017**, *17*, 2381.
- [35] T. Boker, R. Severin, A. Muller, C. Janowitz, R. Manzke, D. Voss, P. Kruger, A. Mazur, J. Pollmann, *Phys. Rev. B* **2001**, *64*, 235305.
- [36] J. Y. Lim, A. Pezeshki, S. Oh, J. S. Kim, Y. T. Lee, S. Yu, D. K. Hwang, G. H. Lee, H. J. Choi, S. Im, *Adv. Mater.* **2017**, *29*, 1701798.
- [37] L. Zhou, K. Xu, A. Zubair, A. D. Liao, W. J. Fang, F. P. Ouyang, Y. H. Lee, K. Ueno, R. Saito, T. Palacios, J. Kong, M. S. Dresselhaus, *J. Am. Chem. Soc.* **2015**, *137*, 11892.
- [38] W. Z. Yu, S. J. Li, Y. P. Zhang, W. L. Ma, T. Sun, J. Yuan, K. Fu, Q. L. Bao, *Small* **2017**, *13*, 1700268.

- [39] I. Amit, T. J. Octon, N. J. Townsend, F. Reale, C. D. Wright, C. Mattevi, M. F. Craciun, S. Russo, *Adv. Mater.* **2017**, *29*, 1605598.
- [40] Y. Huang, E. Sutter, J. T. Sadowski, M. Cotlet, O. L. A. Monti, D. A. Racke, M. R. Neupane, D. Wickramaratne, R. K. Lake, B. A. Parkinson, P. Sutter, *ACS Nano* **2014**, *8*, 10743.
- [41] J. Xia, D. D. Zhu, L. Wang, B. Huang, X. Huang, X. M. Meng, *Adv. Funct. Mater.* **2015**, *25*, 4255.
- [42] C. X. Zhang, C. Gong, Y. F. Nie, K. A. Min, C. P. Liang, Y. J. Oh, H. J. Zhang, W. H. Wang, S. Hong, L. Colombo, R. M. Wallace, K. Cho, *2D Mater.* **2017**, *4*, 015026.
- [43] H. J. Chuang, X. B. Tan, N. J. Ghimire, M. M. Perera, B. Chamlagain, M. M. C. Cheng, J. Q. Yan, D. Mandrus, D. Tomanek, Z. X. Zhou, *Nano Lett.* **2014**, *14*, 3594.
- [44] Y. Liu, H. Wu, H. C. Cheng, S. Yang, E. B. Zhu, Q. Y. He, M. N. Ding, D. H. Li, J. Guo, N. O. Weiss, Y. Huang, X. F. Duan, *Nano Lett.* **2015**, *15*, 3030.
- [45] W. Choi, N. Choudhary, G. H. Han, J. Park, D. Akinwande, Y. H. Lee, *Mater. Today* **2017**, *20*, 116.
- [46] P. Chaisakul, D. Marris-Morini, J. Frigerio, D. Chrastina, M. S. Rouified, S. Cecchi, P. Crozat, G. Isella, L. Vivien, *Nat. Photonics* **2014**, *8*, 482.
- [47] J. Michel, J. F. Liu, L. C. Kimerling, *Nat. Photonics* **2010**, *4*, 527.
- [48] R. Kirchain, L. Kimerling, *Nat. Photonics* **2007**, *1*, 303.
- [49] R. T. Lu, C. Christianson, A. Kirkeminde, S. Q. Ren, J. D. Wu, *Nano Lett.* **2012**, *12*, 6244.
- [50] M. G. Gong, Q. F. Liu, B. Cook, B. Kattel, T. Wang, W. L. Chan, D. Ewing, M. Casper, A. Stramel, J. Z. Wu, *ACS Nano* **2017**, *11*, 4114.
- [51] Y. P. Gong, P. Adhikari, Q. F. Liu, T. Wang, M. G. Gong, W. L. Chan, W. Y. Ching, J. D. Wu, *ACS Appl. Mater. Interfaces* **2017**, *9*, 11016.
- [52] C. Soci, A. Zhang, B. Xiang, S. A. Dayeh, D. P. R. Aplin, J. Park, X. Y. Bao, Y. H. Lo, D. Wang, *Nano Lett.* **2007**, *7*, 1003.
- [53] V. A. Fonoberov, A. A. Balandin, *J. Nanoelectron. Optoelectron.* **2006**, *1*, 19.
- [54] L. Britnell, R. V. Gorbachev, R. Jalil, B. D. Belle, F. Schedin, A. Mishchenko, T. Georgiou, M. I. Katsnelson, L. Eaves, S. V. Morozov, N. M. R. Peres, J. Leist, A. K. Geim, K. S. Novoselov, L. A. Ponomarenko, *Science* **2012**, *335*, 947.
- [55] T. Das, H. Jang, J. B. Lee, H. Chu, S. D. Kim, J. H. Ahn, *2D Mater.* **2015**, *2*, 044006.
- [56] M. S. Long, A. Y. Gao, P. Wang, H. Xia, C. Ott, C. Pan, Y. J. Fu, E. F. Liu, X. S. Chen, W. Lu, T. Nilges, J. B. Xu, X. M. Wang, W. D. Hu, F. Miao, *Sci. Adv.* **2017**, *3*, e1700589.
- [57] G. X. Su, V. G. Hadjiev, P. E. Loya, J. Zhang, S. D. Lei, S. Maharjan, P. Dong, P. M. Ajayan, J. Lou, H. B. Peng, *Nano Lett.* **2015**, *15*, 506.
- [58] D. Yang, B. Li, C. Hu, H. Deng, D. D. Dong, X. K. Yang, K. K. Qiao, S. J. Yuan, H. S. Song, *Adv. Opt. Mater.* **2016**, *4*, 419.